

This is a repository copy of *Transformation-induced changes in the DNA-nuclear matrix interface, revealed by high-throughput analysis of DNA halos*.

White Rose Research Online URL for this paper:

<https://eprints.whiterose.ac.uk/117872/>

Version: Accepted Version

Article:

Wilson, Rosemary and Coverley, Dawn Alison orcid.org/0000-0001-8262-7023 (2017) Transformation-induced changes in the DNA-nuclear matrix interface, revealed by high-throughput analysis of DNA halos. Scientific Reports. ISSN 2045-2322

<https://doi.org/10.1038/s41598-017-06459-7>

Reuse

Items deposited in White Rose Research Online are protected by copyright, with all rights reserved unless indicated otherwise. They may be downloaded and/or printed for private study, or other acts as permitted by national copyright laws. The publisher or other rights holders may allow further reproduction and re-use of the full text version. This is indicated by the licence information on the White Rose Research Online record for the item.

Takedown

If you consider content in White Rose Research Online to be in breach of UK law, please notify us by emailing eprints@whiterose.ac.uk including the URL of the record and the reason for the withdrawal request.

Transformation-induced changes in the DNA-nuclear matrix interface, revealed by high-throughput analysis of DNA halos.

Rosemary H.C. Wilson^{1,2,*} and Dawn Coverley¹

¹ Department of Biology, University of York, Heslington, York, UK, YO10 5DD

² Current address: Sir William Dunn School of Pathology, University of Oxford, South Parks Road, Oxford, UK, OX3 1RE

*Correspondence: rosemary.wilson@path.ox.ac.uk Tel: +44-(0)1865-618651

Running title Analysis of changes in chromatin loops

Word count 2886 not including acknowledgements, abstract and legends

Key words Chromatin loop, Maximum Fluorescence Halo Radius, Nuclear Matrix, Cancer

Abstract In higher eukaryotic nuclei, DNA is periodically anchored to an extraction-resistant protein structure, via matrix attachment regions. We describe a refined and accessible method to non-subjectively, rapidly and reproducibly measure both size and stability of the intervening chromatin loops, and use it to demonstrate that malignant transformation compromises the DNA-nuclear matrix interface.

Introduction The three-dimensional organization of chromatin plays a central role in the regulation of nuclear functions. Organization includes periodic attachment to a biochemically-defined, extraction-resistant structure referred to as the nuclear matrix (NM), via Scaffold or Matrix Attached Regions of DNA (S/MARs). However, despite extensive analysis of S/MAR sequences and evidence that replication and transcription take place at the base of chromatin loops, the concept of a NM is not universally accepted, and has been under investigated. As a result, we have limited information on the changing relationship between chromatin and the NM during development and disease¹ and a very limited understanding of the functional significance of pathology-associated changes in nuclear structure². The Maximum Fluorescence Halo Radius (MFHR) method³ has the potential to reveal information about the relative role of loop-base attachments in different cell types. It allows visualization and measurement of loops and the residual nucleus (RN), after unpackaging by removal of histones and other associated proteins, whilst maintaining NM attachment (**Fig. 1a**). It has been used to investigate average chromatin loop size^{4,5}, NM attachment of individual genes^{6,7} the effect of replication rate^{3,8,9}, and of knockdown of specific proteins^{10,11}. However, its full potential to follow changes in chromatin loops has not been realized because traditional methods for analysis of halo images are labor intensive, rely on subjective visual assessment of radius measurements and are vulnerable to user variability. Moreover, typically only defined halo structures are quantified which omits important information about populations of cells. We have developed an accessible MFHR image analysis method and established a straightforward procedure to set threshold parameters. Halo Image Macro (HIM), used with NIH ImageJ¹², enables rapid, non-subjective quantification of average DNA loop size in populations, calculated from the shape of the whole DNA halo. We have also developed related assays that report on loop stability (**Supplementary table 1**), and applied these to reveal oncogene-induced changes in the chromatin-NM interface. MFHR is a conceptually simple but technically challenging method, which has the potential to return valuable data about an under-investigated area of cell biology.

Results

Establishment of MFHR halo edge thresholds for image analysis Accurate quantification of mean chromatin loop size is based on establishment of two 'edges'; the outer threshold of the halo and the residual nucleus (RN) (**Fig. 1a**). Firstly we establish the correct exposure for MFHR image capture using RN size, by calibrating settings to the area occupied by the NM. We use a GFP-tagged NM protein (EGFP-CIZ1 C-term274¹³) to mark the NM, and set

MFHR image exposure. For our apparatus 5ms returns a mean value for RN radius that is 100.3 % of CIZ1 NM radius (**Fig. 1b**).

So that the pixel intensity threshold that specifies the edge of the RN is compatible with the wide range of intensities within a population of MFHR processed cells (**Supplementary Fig. 1a**), we use an RN threshold that is related to individual image maxima. To select the RN threshold, RN radius measurements returned by HIM with a range of settings are compared to those generated by visual assessment of the RN boundary, for a training set of images. In the following experiments we use an RN equal to the local maxima less 55 ($x=55$), which returned 101 % of visual estimates of the training set (**Fig. 1c, Supplementary Fig. 1b**).

The pixel intensity for the outer threshold is more difficult to determine visually, and is subject to both user and screen variability (**Supplementary Fig. 1c**). Unless indicated, we use an absolute pixel intensity threshold of 15, which captures $\geq 95\%$ of the area under the curve and confidently includes the outermost DNA loop edge across a population of cells (**Fig. 1d, e, Supplementary Fig. 1d**).

With a fixed image capture time, established RN and outer thresholds, HIM is capable of systematic comparison of multiple large data sets and automatically returns linked measurements for RN area and total area, for batches of submitted images (**Supplementary Fig. 1e**). Straightforward calculations convert these to halo radius (see User Guide).

Cell lines derived from high grade tumors exhibit destabilized halos Comparing halo size within a set of breast and bladder derived cell lines revealed considerable variation between populations (**Fig. 1f**). Moreover, all cell types gave rise to two classes of product, differing in their RN. Class I have defined RNs while class II have a poorly defined RN and fail to be measured by HIMx55/15 (**Fig. 1g, h**). A bright, well defined RN reflects greater retention of DNA within the residual nucleus and implies strong DNA:NM attachments that withstand the extraction process. Class I cells can be further divided into Ia (bright RN) or Ib (pale RN) using a specialized HIM (**Supplementary Fig. 2**). In fact most published MFHR analyses do not comment on class differences, measuring only defined and regular MFHR entities (and showing only class Ia cells), thereby under-reporting differences between populations.

Notably class distribution, determined by RN HIM, is significantly different between the poorly differentiated breast and bladder cancer cell lines MDA-MB-231 and T24/EJ, compared to lower grade tumor-derived lines, or cells derived from normal urothelial tissue.

This manifests as increased class Ib and class II cells (**Fig. 1g**), and suggests that destabilization of the DNA:NM interface is a feature of malignant transformation.

Effect of introduced oncogenes To interrogate this under more defined conditions we used an isogenic Mesenchymal Stem Cell (MSC) series, with sequential introduction of five well-characterized oncogenes¹⁴ (**Fig. 2** and **Supplementary Figure 3a**). Variation between the five populations, necessitated careful selection of HIM thresholds to support measurement of cells over the whole series under the same conditions (**Supplementary Fig. 3**). Range from local maxima was selected for both RN and outer threshold (x75/x180), generating data that reflect both chromatin loop size and RN intensity. This revealed significant shifts toward larger and more diffuse halos after expression of HPV-E6 (50% increase in mean halo size and 4 fold decrease in class Ia cells), and again after expression of H-Ras (111% increase in size and 3 fold increase in class II cells), compared to the starting population (**Fig. 2a, b**). In contrast, neither HPV-E7, nor SV40 small-t antigen had a measureable impact on either parameter. A second set of HIM parameters that use an absolute outer threshold (x75/15), making size determination independent of RN intensity, confirmed that halo radius is affected by H-Ras expression (**Fig. 2c**). However, the effect of E6 was not observed, suggesting that it likely reflects a complex effect on structure of the NM itself (RN). Consistent with this, larger RN sizes were recorded following E6 expression (**Supplementary Fig. 3h**).

Stability of MFHR halos in five-member isogenic transformation series DNA halos are unstable structures so that class I halos transition to class II halos over time. The wavelength used to image ethidium bromide-stained halos (546 nm excitation) induces DNA damage¹⁵⁻¹⁸, by introducing both double and single strand breaks. Cells that start with a bright RN and have more DNA associated to the nuclear matrix (class Ia) appear to withstand more stochastic damage before DNA is released and can diffuse away. This instability limits image capture time but, by applying HIM with an outer threshold related to the local maxima, it also offers a means to measure dynamic changes in halo stability (**Fig. 2d, e**). As DNA is fragmented and lost, the intensity drops until a threshold is reached when the outer edge of a halo can no longer be measured (<180 for HIMx75/x180), and a cell 'fails' to return a value (**Fig. 2d**). By comparing a series of images captured over 60s, we can classify halos into stable or rapidly decaying entities, allowing time to decay and percentage of surviving halos to be plotted. This shows that halos are much more stable in MSC1 cells than in MSC5 cells (**Fig. 2e, f**). Similar results were obtained for high-grade tumour cell lines MDA-MB-231 and T24/EJ (HIMx55/x240), compared to lower grade cells (**Fig. 2g, h**). Partial release of loop

DNA from the NM, and differential stability, has been noted previously but has not been quantified¹⁹.

Discussion

The isogenic MSC cell series used here are characterised by acquisition of malignant phenotype upon expression of defined oncogenes. Most notably, anchorage independent growth and tumour formation in mice both increase dramatically upon introduction of the GTPase H-Ras into MSC4 cells (which already harbour HPV-E6, HPVE7 and small t-antigen) to generate MSC5 cells¹⁴. In our experiments introduction of H-RAS, which bypasses growth factor regulation, initiates a transition toward larger halos, identifying changes in S/MAR recruitment as co-regulated with these malignant characteristics. Induced expression of H-Ras has been previously linked with changes in the protein component of the NM and DNA supercoiling²⁰, offering some precedent for these findings. We also show that HPV-E6 which inactivates the tumor suppressor p53, initiates a separate transition in size, stability and class, all of which suggest fewer or shorter interface between DNA and the NM. Both HPV E6 protein and viral DNA are found associated with the NM²¹, however, there is no further evidence to support a direct link with stability or structure of the nucleus.

Neither H-Ras or E6 are reported to increased proliferation rate in this MSC series, compared to their parent line (though introduction of t-antigen to generate MSC4 did¹⁴), arguing that DNA:NM stability is not directly related to proliferation rate. This is important because cell cycle distribution might be expected to impact on the DNA:NM interface when replication origins are recruited to the NM during initiation of DNA replication¹. In fact published work²², and our own analysis (not shown), which compared unsynchronised cells, and G1 or S-phase cells did not support global MFHR loop size differences during the mitotic cell cycle.

There has been some genome wide analysis of NM-attached DNA in two of the breast-derived lines used here²³, which reports differences that compare well with our results. Specifically, in MCF10A cells NM-DNA was more likely to map to gene rich regions and to expressed genes than in MDA-MB-231, where NM-DNA was enriched in non-expressed genes. However, in both lines H3K4me3, H3K27me3 and H3K9me2 were appropriately associated with expressed and non-expressed genes, suggesting that NM attachment is not closely related to epigenetic landscape. The relationship may not be clear cut however, because analysis of methylation status of LINE1 and Sat2 elements in the MSC1-5 cell series revealed hypomethylation in the MSC5 line²⁴. Though a direct correlation between this

study of DNA methylation and our study of NM-attachment cannot be drawn, DNA methylation of specific S/MARs has been reported to affect function²⁵.

The molecular basis for the increases in loop size and decrease in stability remains to be determined. Clearly, global changes in transcription rate, reported in cancer cells²⁶, could affect the DNA:NM interface, and there are numerous published examples of tumour-associated changes in nuclear matrix protein composition^{2,27-30} or sub-nuclear architecture at the level of domain organization². Moreover, there are specific examples of diseases that are associated with loss of S/MAR sequences³¹. Despite the strong correlation between degeneration of nuclear architecture and cancer, there is little evidence that distinguishes cause and effect. Loss of stabilizing architecture could facilitate loss of cellular identity through relaxation of spatial control over gene expression³⁰, or reduced anchorage of chromatin loops might directly support emergence of genome instability through inaccurate repair of strand breaks. Alternatively, loss of stable structure is a consequence of cancer-associated changes in gene expression. Here we present evidence that introduction of a transforming oncogene *causes* (directly or indirectly) disruption of the DNA:NM interface. Moreover, the approach described here offers a well-defined methodology with which to further dissect malignancy-associated changes in nuclear structure, starting with the previously unrecognised trigger, H-Ras.

Methods

Cells and cell culture Cells were obtained from ATCC or JCRB cell banks and grown on glass coverslips to 50-70 % confluence, as recommended. Sequentially transformed mesenchymal stem cells¹⁴ (MSC) were kindly provided by Dr Juan Funes and Prof Chris Boshoff, and normal human urothelial cells (NHU), derived from tissue biopsies³², by Edward Bowen and Prof Jennifer Southgate. Breast cell lines were derived from normal breast tissue (MCF10A³³), low grade breast cancer (MCF7³⁴) or oestrogen receptor negative metastatic breast cancer (MDA-MB-231³⁵). Bladder cell lines were from metastatic bladder cancer (T24/EJ³⁶) or lower grade bladder cancers (RT4 and RT112³⁶).

Maximum Fluorescence Halo Radius extraction method The ethidium bromide MFHR method has been described previously^{4,9}. For the analysis performed here, the following changes were made: 0.25 % Igepal (NP40 substitute, Fluka 56741) was used instead of 0.5 % NP40, and a development incubation was included (5 mins in the dark) to enable halos to reach a stable expanded state prior to imaging. All incubations were performed on ice using ice-cold buffers. Briefly, cells on coverslips were washed in D-PBS followed by 1 min

incubation in detergent extraction buffer (0.25 % Igepal, 10 mM MgCl₂, 0.5 mM CaCl₂, 50 mM Tris-Cl pH 7.5). Coverslips were then incubated for 30 s in series in each of 0.5 M NaCl, 1.0 M NaCl and 1.5 M NaCl extraction buffers, followed by 2.0 M NaCl extraction buffer (all made up in 0.2 mM MgCl₂, 10 mM Tris-Cl pH 7.5). The last incubation lasts for 2 min, including 1 min exposure to 240 nm UV treatment, and is done in the presence of 100 µg/ml ethidium bromide. Coverslips were then mounted on slides, sealed with nail varnish and matured in the dark for 5 min.

Microscopy and image capture Halos were imaged using a Zeiss Axiovert 200M fluorescent microscope using Zeiss filter set 15 (Excitation filter: band pass 546/12 nm, Emission filters: beam splitter 580 nm and emission long pass 590 nm) and AxioCam HRm digital camera with Openlab software (PerkinElmer). Images were acquired using constant exposure (5ms unless stated otherwise), taking care to image only 'fresh' fields that were not previously viewed. 50-80 images (RGB 8-bit, file size 1388 x 1040 pixels) were acquired from each sample, within 10 min of preparation. Raw Openlab LIFF files were saved for reference but files were transferred with no additional processing as RGB 8-bit TIFF files for analysis in ImageJ.

Visual size estimates For analysis by eye, MFHR files were opened in ImageJ 1.46 for Mac OS X (NIH). Halo areas were calculated using the 'polygon' function to draw around the whole of the visible RN and halo (**Supplementary Fig. 1b**), quantified using the 'measure' function, and radius measurements derived using the formula in HIM User Guide. Alternatively halo radius measurements were estimated using the 'line' function to draw a vertical line from the outer edge of the RN to the outer edge of the visible halo, at the lowest position in each image (**Supplementary Fig. 1b**), followed by the 'measure' function. Irregularities in structure have significantly more impact when using a single radius measurement.

Halo Image Macro (HIM) analysis Image files were processed using ImageJ macro HIM to calculate average halo radius, class percentages or stability of halos as described. HIM versions for each type of analysis are indicated in main text and see **Supplementary Table 1**. HIM set up and validation is described in results and supplementary information. Briefly, HIM defines RN and outer halo edges, creating an ROI for both regions. HIM matches RN and outer regions where possible using halo positional information. Output is a RN threshold analysis picture and outer threshold analysis picture for each image, and a .csv file containing RN and outer area measurements. Users then derive the halo radius. MSC cell

lines were processed for halo radius size using HIM x75/15 or HIM x75/x180 as indicated. Other cell lines were processed for halo radius analysis using HIM x55/15.

Using HIM to calculate halo class distribution In addition to a range of halo diameters, populations of cells processed by MFHR return two classes of product (**Fig. 1h**). Class I have defined RNs and class II have an ill-defined RN with poor structure. Class I is further subdivided into Ia (bright) where >50% of the returned RN from local maxima is above 220 intensity and Ib (pale) where <50% of their RN above 220 intensity. Visual designation can be subject to user variability (not shown), therefore we designed a specialised classification HIM (RN HIM) which uses RN intensity to non-subjectively classify halos into class Ia, Ib or II (**Supplementary Fig. 2, 3, Supplementary Table 1**). MSC cell lines were processed for classification analysis using HIM RNx75/RN220, other cell lines were processed using HIM RNx55/RN220.

Using HIM to measure stability For halo size the time each halo is exposed to light before/during imaging is 1-2 seconds, therefore the opportunity for halo degradation is minimal. In contrast, for stability measurements, halos are imaged through a 60 second window to reveal time-dependent decay, as seen in figure 2d-h. A series of images collected over time can be used to quantify stability and rate of halo decay. We typically collect 7 images of individual cells from 0 s to 60 s at 10 s intervals using 546 nm light (see microscopy and image capture), typically from 8 cells per coverslip for at least four coverslips. Users should decide if they wish to sample from the whole population or from one class. After curation (identification of whole image ROIs derived from failed cells), we plotted surviving halos as percentage of the population for each time point. Alternatively, halo failure time can be used to plot average time to decay. Where halos did not fail, and remained measureable at 60s, they were given a fail time of 70s. MSC cell lines were processed using HIM x75/x180, other cell lines were processed using HIM x55/x240.

Western blotting Whole cell lysates were generated from asynchronously growing MSC cells, cultured as recommended¹⁴. Equal amount of sample were run on SDS-PAGE and transferred to 0.1 µm nitrocellulose before being probed for introduced oncogenes, to validate MSC cell line identity. Antibodies used were mouse anti-PCNA (PC10, abcam), rabbit anti-HRAS (18295-1-AP, Proteintech), E6 (N17, Santa Cruz) and mouse anti-actin (A4700, Sigma) as a loading control.

Sample numbers and statistics Mean halo radius data, classification data and stability data were generated from image sets derived from four coverslips, comprising two technical

replicates from each of two biological replicates. Stability data are presented as percentage of surviving halos at each time point or average time to decay. These were typically generated from 32 cells, comprising 8 cells (each followed for 60s) from each coverslip. All error bars are SEM. Powers were calculated using Student's t-test, where * $p < 0.05$, ** $p < 0.005$, *** $p < 0.0005$.

Supplementary information More detailed descriptions of the setup and validation of HIM methods are included in supplementary information, as well as a HIM user guide.

Acknowledgements We thank Chris Boshoff and Juan Funes for sharing their powerful MSC cell series, and Jennifer Southgate and Edward Bowen for providing NHU cells. We thank Amanda Collier for help with data collection, Roger Leigh and Nick McEntyre for help with ImageJ, Gillian Higgins for technical support, and Dimitris Lagos, Sandy MacDonald and Justin Ainscough for critical comments on the manuscript. This work was funded by the UK Biotechnology and Biological Sciences Research Council Doctoral Training Fellowship to RW.

References

1. Wilson, R.H. & Coverley, D. Relationship between DNA replication and the nuclear matrix. *Genes Cells* **18**, 17-31 (2013).
2. Zink, D., Fischer, A.H. & Nickerson, J.A. Nuclear structure in cancer cells. *Nat Rev Cancer* **4**, 677-687 (2004).
3. Vogelstein, B., Pardoll, D.M. & Coffey, D.S. Supercoiled loops and eucaryotic DNA replicaton. *Cell* **22**, 79-85 (1980).
4. Buongiorno-Nardelli, M., Micheli, G., Carri, M.T. & Marilley, M. A relationship between replicon size and supercoiled loop domains in the eukaryotic genome. *Nature* **298**, 100-102 (1982).
5. Trevilla-Garcia, C. & Aranda-Anzaldo, A. Cell-type-specific organization of nuclear DNA into structural looped domains. *J Cell Biochem* **112**, 531-540 (2011).
6. Heng, H.H., *et al.* Chromatin loops are selectively anchored using scaffold/matrix-attachment regions. *J Cell Sci* **117**, 999-1008 (2004).
7. Gerdes, M.G., Carter, K.C., Moen, P.T., Jr. & Lawrence, J.B. Dynamic changes in the higher-level chromatin organization of specific sequences revealed by in situ hybridization to nuclear halos. *J Cell Biol* **126**, 289-304 (1994).
8. Courbet, S., *et al.* Replication fork movement sets chromatin loop size and origin choice in mammalian cells. *Nature* **455**, 557-560 (2008).
9. Lemaitre, J.M., Danis, E., Pasero, P., Vassetzky, Y. & Mechali, M. Mitotic remodeling of the replicon and chromosome structure. *Cell* **123**, 787-801 (2005).
10. Guillou, E., *et al.* Cohesin organizes chromatin loops at DNA replication factories. *Genes Dev* **24**, 2812-2822 (2010).
11. Yamazaki, S., *et al.* Rif1 regulates the replication timing domains on the human genome. *EMBO J* **31**, 3667-3677 (2012).
12. Schneider, C.A., Rasband, W.S. & Eliceiri, K.W. NIH Image to ImageJ: 25 years of image analysis. *Nat Methods* **9**, 671-675 (2012).
13. Ainscough, J.F., *et al.* C-terminal domains deliver the DNA replication factor Ciz1 to the nuclear matrix. *J Cell Sci* **120**, 115-124 (2007).
14. Funes, J.M., *et al.* Transformation of human mesenchymal stem cells increases their dependency on oxidative phosphorylation for energy production. *Proc Natl Acad Sci U S A* **104**, 6223-6228 (2007).
15. Solarczyk, K.J., Zarebski, M. & Dobrucki, J.W. Inducing local DNA damage by visible light to study chromatin repair. *DNA repair* **11**, 996-1002 (2012).
16. Ferrando-May, E., *et al.* Highlighting the DNA damage response with ultrashort laser pulses in the near infrared and kinetic modeling. *Frontiers in genetics* **4**, 135 (2013).
17. Gassman, N.R. & Wilson, S.H. Micro-irradiation tools to visualize base excision repair and single-strand break repair. *DNA repair* **31**, 52-63 (2015).
18. Zarebski, M., Wiernasz, E. & Dobrucki, J.W. Recruitment of heterochromatin protein 1 to DNA repair sites. *Cytometry. Part A : the journal of the International Society for Analytical Cytology* **75**, 619-625 (2009).
19. Maya-Mendoza, A., Hernandez-Munoz, R., Gariglio, P. & Aranda-Anzaldo, A. Natural ageing in the rat liver correlates with progressive stabilisation of DNA-nuclear matrix interactions and withdrawal of genes from the nuclear substructure. *Mech Ageing Dev* **126**, 767-782 (2005).
20. Malyapa, R.S., Wright, W.D., Taylor, Y.C. & Roti Roti, J.L. DNA supercoiling changes and nuclear matrix-associated proteins: possible role in oncogene-mediated radioresistance. *Int J Radiat Oncol Biol Phys* **35**, 963-973 (1996).
21. Chen, H.B., *et al.* Human papillomavirus 16 E6 is associated with the nuclear matrix of esophageal carcinoma cells. *World J Gastroenterol* **7**, 788-791 (2001).
22. Jackson, D.A., Dickinson, P. & Cook, P.R. The size of chromatin loops in HeLa cells. *Embo j* **9**, 567-571 (1990).

23. Dobson, J.R., *et al.* Identifying Nuclear Matrix-Attached DNA Across the Genome. *Journal of cellular physiology* **232**, 1295-1305 (2017).
24. Wild, L., Funes, J.M., Boshoff, C. & Flanagan, J.M. In vitro transformation of mesenchymal stem cells induces gradual genomic hypomethylation. *Carcinogenesis* **31**, 1854-1862 (2010).
25. Kisseljova, N.P., *et al.* DNA polymorphism and epigenetic marks modulate the affinity of a scaffold/matrix attachment region to the nuclear matrix. *European journal of human genetics : EJHG* **22**, 1117-1123 (2014).
26. Bywater, M.J., Pearson, R.B., McArthur, G.A. & Hannan, R.D. Dysregulation of the basal RNA polymerase transcription apparatus in cancer. *Nat Rev Cancer* **13**, 299-314 (2013).
27. He, S., *et al.* Chromatin organization and nuclear microenvironments in cancer cells. *J Cell Biochem* **104**, 2004-2015 (2008).
28. Albrethsen, J., Knol, J.C. & Jimenez, C.R. Unravelling the nuclear matrix proteome. *Journal of proteomics* **72**, 71-81 (2009).
29. Lever, E. & Sheer, D. The role of nuclear organization in cancer. *The Journal of pathology* **220**, 114-125 (2010).
30. Munkley, J., *et al.* Cyclin E is recruited to the nuclear matrix during differentiation, but is not recruited in cancer cells. *Nucleic Acids Res* **39**, 2671-2677 (2011).
31. Bode, J., Benham, C., Knopp, A. & Mielke, C. Transcriptional augmentation: modulation of gene expression by scaffold/matrix-attached regions (S/MAR elements). *Critical reviews in eukaryotic gene expression* **10**, 73-90 (2000).
32. Southgate, J., Hutton, K.A., Thomas, D.F. & Trejdosiewicz, L.K. Normal human urothelial cells in vitro: proliferation and induction of stratification. *Lab Invest* **71**, 583-594 (1994).
33. Tait, L., Soule, H.D. & Russo, J. Ultrastructural and immunocytochemical characterization of an immortalized human breast epithelial cell line, MCF-10. *Cancer Res* **50**, 6087-6094 (1990).
34. Brooks, S.C., Locke, E.R. & Soule, H.D. Estrogen receptor in a human cell line (MCF-7) from breast carcinoma. *J Biol Chem* **248**, 6251-6253 (1973).
35. Cailleau, R., Olive, M. & Cruciger, Q.V. Long-term human breast carcinoma cell lines of metastatic origin: preliminary characterization. *In Vitro* **14**, 911-915 (1978).
36. Southgate, J., Proffitt, J., Roberts, P., Smith, B. & Selby, P. Loss of cyclin-dependent kinase inhibitor genes and chromosome 9 karyotypic abnormalities in human bladder cancer cell lines. *Br J Cancer* **72**, 1214-1218 (1995).

Author Contribution statement RW developed the analysis method, and collected and analyzed the data, RW and DC designed experiments and wrote the manuscript.

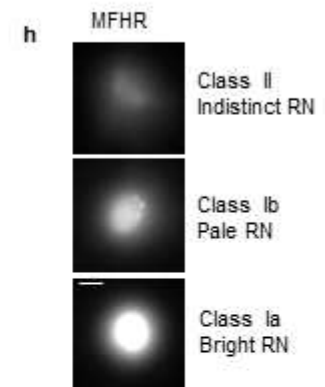
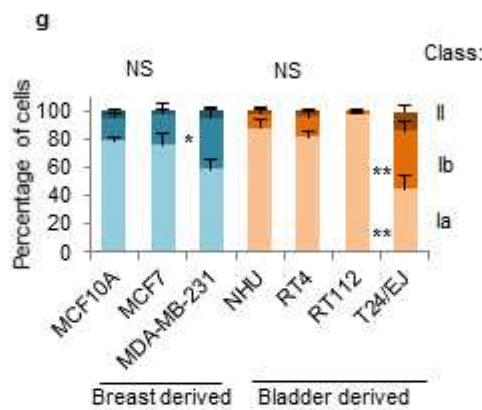
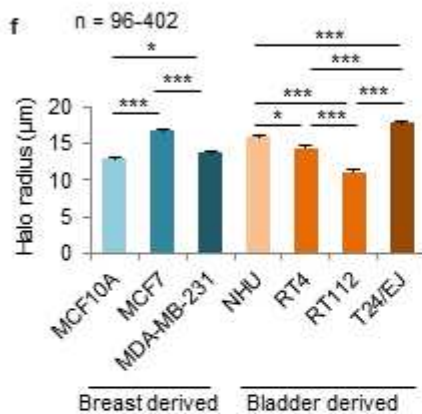
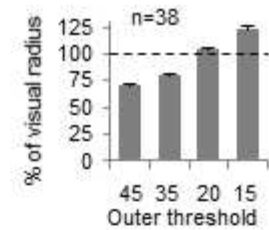
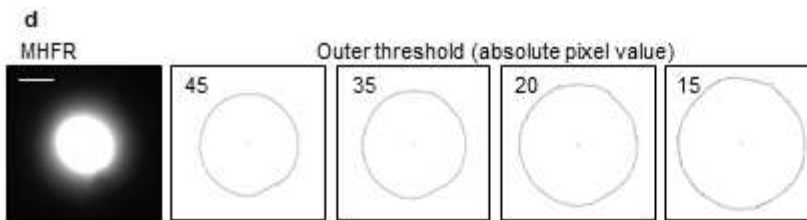
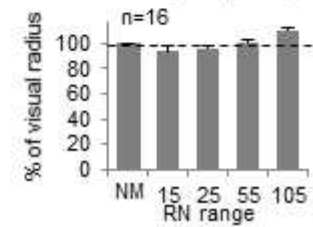
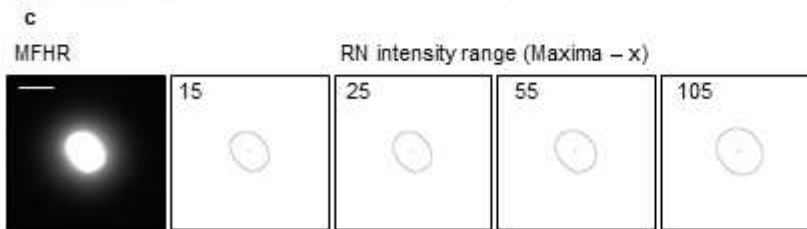
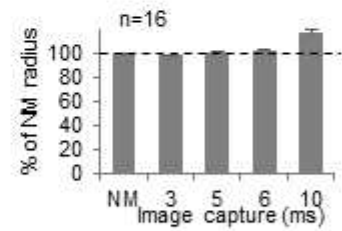
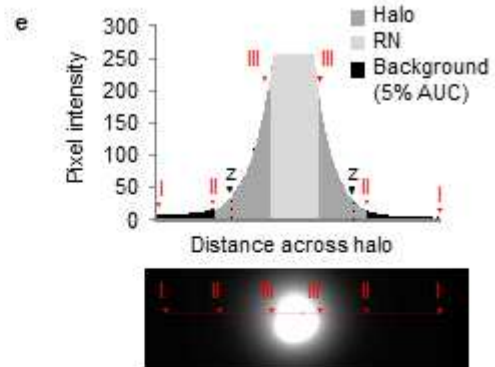
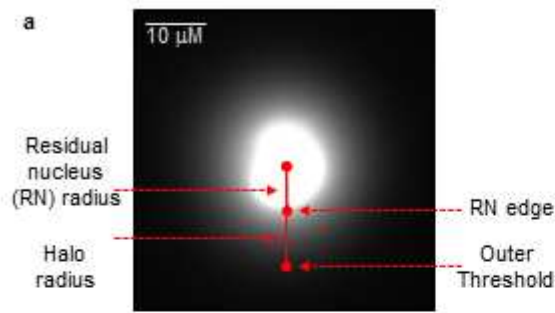
Additional Information The authors declare no competing financial interests.

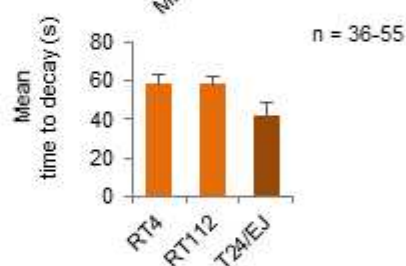
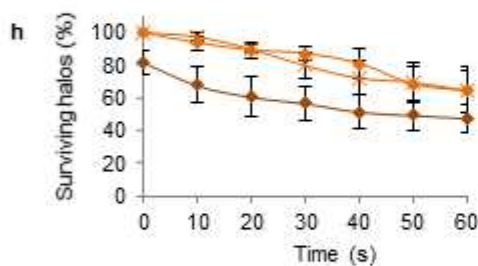
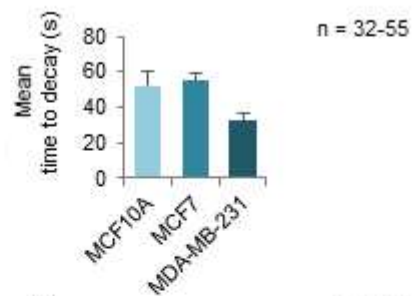
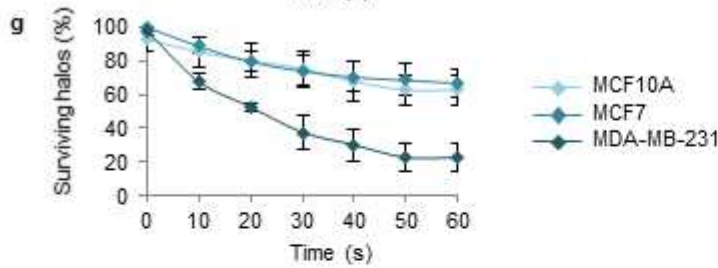
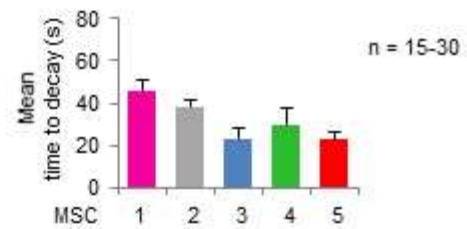
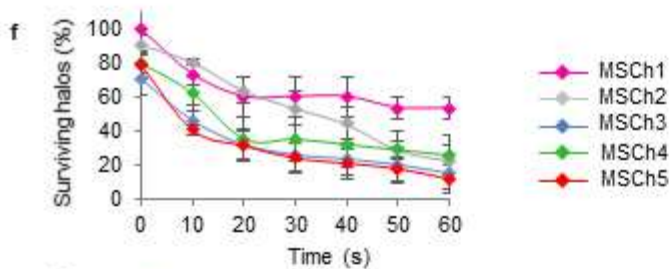
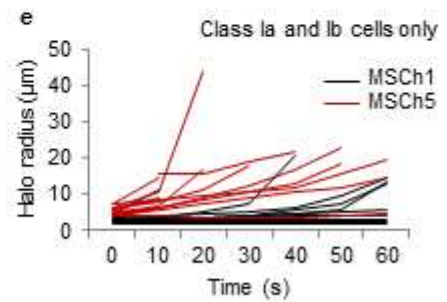
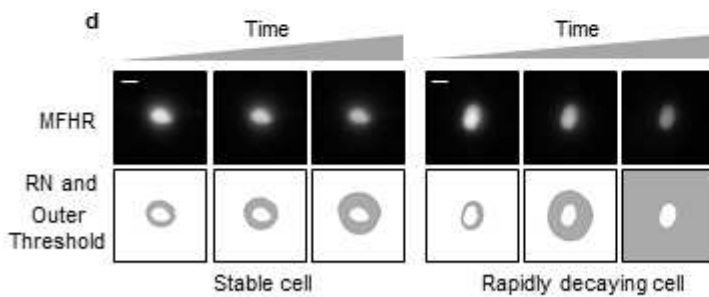
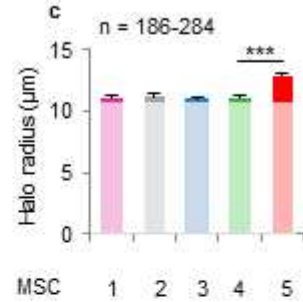
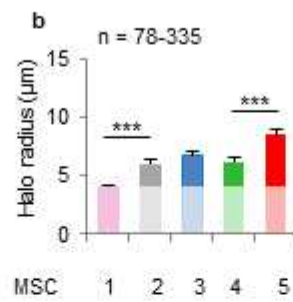
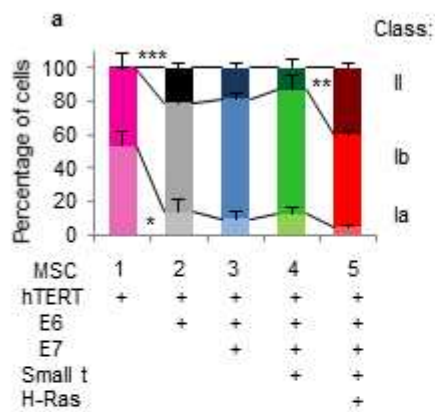
Figure legends

Figure 1: Calibration and edge determination. a) Example MFHR image. b) NM marker (green) and DNA in MFHR-extracted nuclei (white). Histogram shows mean RN radius as percentage of NM marker, +SEM. c) RN and d) outer threshold positions, determined by HIM, using indicated pixel threshold values. Histograms show mean derived radius as percentages of visually-derived values. e) Pixel intensity plot across an MFHR-processed

nucleus, showing outer threshold (II), RN threshold (III), and typical outer threshold estimated by eye (z). f) Mean halo radius and g) class distribution for indicated cell lines, +SEM. h) Examples of class Ia, Ib and II MFHR-processed cells.

Figure 2: Transformation-induced changes in chromatin loop size and stability. a) Class distribution for Mesenchymal Stem Cell (MSC) series, with introduction of the indicated oncogenes¹⁴. b) Mean halo radius using HIM x75/x180 or c) HIM x75/15. d) Example MFHR stability over time, showing edges determined by HIM x75/x180. e) Halo measurements over 60s time-course for individual MSC1 and MSC5 cells. f) Stability measurements plotted as percentage of surviving halos (left), and average time to decay (right). g) and h), as in f, for breast and bladder-derived cell lines respectively. i) Possible effects of transformation on DNA:NM interface.





Supplementary Information for:

Transformation-induced changes in the DNA-nuclear matrix interface, revealed by high-throughput analysis of DNA halos.

Rosemary H.C. Wilson^{1,2,*} and Dawn Coverley¹

¹ Department of Biology, University of York, Heslington, York, UK, YO10 5DD

² Current address: Wellcome Trust Centre for Human Genetics, University of Oxford, Roosevelt Drive, Oxford, UK, OX3 7BN

*Correspondence: rosemary.wilson@well.ox.ac.uk Tel: +44-(0)1865-287719

Legends to supplementary figures

Supplementary figure 1: Validation of HIM a) Pixel intensity plots across example MFHR images, showing intensities across the whole of the image (upper), flattening out over the higher intensity RNs. The lower plot shows captured RNs after application of local maxima less 55 (x55) threshold. Plots show representative sample class Ia (RN reaching maximal 255 intensity) and class Ib (RN maxima less than 255) images. b) Schematic shows RN and halo boundaries. c) Six data sets extracted from the same population of images, expressed as frequency distribution of halo radius measurements. Results were generated using visual or HIM analysis as indicated, or by different users and screens. d) The effect of RN and outer threshold settings on average halo radius for the same population of images, showing little variation associated with changes in RN threshold intensity setting, and a more dramatic dependence on outer threshold setting. Our default HIM setting of x55/15 is shown in black. e) Schematic shows images produced by ImageJ during HIM process. HIM selects an ROI for the input image (left), using either a threshold related to the local maxima (RN, top set) or an absolute pixel intensity threshold (outer threshold, lower set). The ROI edge is closed and set to 255 (only required for threshold related to local maxima). HIM then measures the ROI area and produces a numbered ROI image (analyse particles). f) Average RN radius, halo radius and total radius for a sample data set of 3T3 cells, shown as mean (upper), or frequency distribution (lower). g) Graphs show pixel intensity across an MFHR treated nucleus (left) and one that was treated only up to 0.5M NaCl, so that histones are not extracted and DNA does not expand beyond the RN. Boundaries selected by HIM x55/15 are indicated.

Supplementary figure 2: HIM based classification of class Ia and Ib halos a) Left: Histogram shows the percentage of the RN area captured by HIM x55/15, that is also captured using an absolute intensity value for RN threshold (as indicated), for a representative set of 3T3 images. This effectively separates class Ia and Ib cells, because for Ia cells the two measurements are similar, and the % is close to 100. RN 220 was selected for separation of class Ia and Ib cells and validated (using HIM RNx55/RN220) by comparing results to visual classification of a 3T3 image training dataset (right). The two outputs were aligned with no 'false Ib' or 'false Ia' (where HIM classification does not match visual assessment). b) Histogram shows mean RN, halo and total radius measurements for class Ia and class Ib 3T3 cells, using x55/15. c) Histogram shows mean halo radius for class Ia, class Ib or both class Ia and b for a set of non-cancer cell lines, using x55/15. The same trend is observed when independent of class used. d) Histogram shows classification for non-cancer cell lines used in c.

Supplementary figure 3: Customization of HIM for analysis of linked set of MSC lines

a) Western blot validation of MSC lines 1-5 showing introduced oncogenes as indicated. b) Graph shows RN radius calculated by HIM using the indicated RN thresholds (local maxima less x) for a sample set of MSC1 ($n=100$) and MSC3 ($n=66$) images. Values are plotted as percentage of RN radius calculated using visual assessment. c) Histogram shows average halo radius for MSC1 and 3 cells, with the indicated HIM threshold settings. MSC1 and 3 return a difference regardless of settings. We prefer $x75/x180$ as this allows a greater proportion of cells to return a measurement. For MSC1, $n=41$ with $x55/x240$, $n=44$ with $x75/x240$, $n=83$ with $x75/x180$. For MSC3, $n=2$ with $x55/x240$, $n=2$ with $x75/x240$, $n=16$ with $x75/x180$. d) Graph shows percentage of MSC1 and 3 cells measureable, with the indicated outer thresholds (using constant RN of $x75$). At $x230$ and $x240$ most MSC3 cells fail to return a value. For analysis of the full MSC series, shown in Fig. 2b, $x75/x180$ was applied. e) Establishing settings for classification of Ia and Ib by HIM. Histogram shows the percentage of the captured RN (local maxima less 75) that is also captured when using the indicated absolute intensities for RN, for a representative set of MSC1 images. f) Histogram shows classification of MSC1 images using the indicated HIM parameters compared to visual assessment of the training set. Images that were visually scored to be class Ia but by HIM were scored to be class Ib are defined as 'false Ib', and those visually scored to be Ib but by HIM scored as Ia are defined as 'false Ia'. RN 220 most accurately separates the classes. g) As e) for representative MSC1, MSC3 and MSC5 images, using HIM RN_{x75}/RN_{220} . h) Histogram shows mean RN radius (for class Ia and b) across the MSC series using $HIM_{x75}/15$, also used to generate the data in Fig. 2c.

Supplementary figure 4: Analysis of variance for MSC lines

a) Frequency distribution graph shows data for all five MSC cell lines, each combined from four replicate experiments. b) Frequency distribution graph shows individual replicates for MSC1 and MSC2. c) As b for MSC4 and MSC5. d) As b for MSC2 and MSC4. e) Table shows ANOVA results for the indicated groups. f) Histograms show average halo size for MSC1 and MSC4 (left) and MSC4 and MSC5 (right) when pairs were processed together and imaged on the same slide at the same time. Data collected from three replicates for each pair of cell lines. Error bars are SEM, * $p < 0.05$, *** $p < 0.0005$. No significant difference between MSC4 collected with MSC1 or MSC4 collected with MSC5.

Supplementary Methods - ImageJ HIM setup and validation:

RN edge determination In ImageJ, thresholds can be set based on absolute intensity values or at an intensity relative to the local maxima for each individual image. Due to the wide range of maximal intensities within a population of MFHR processed cells, an absolute pixel intensity threshold is usually not applicable to the whole population. In fact, the intensity range within an RN is more similar in a halo population than is the maximal (**Supplementary Fig. 1a**), meaning an RN threshold related to the individual maxima is useful. To set the RN threshold we compared RN radius measurements returned by HIM with different settings, to visual assessment of the RN boundary (**Fig. 1c**, **Supplementary Fig. 1b**), for training images.

Choice of measurements MFHR image files were analysed in ImageJ using HIM, as described in the User Guide. HIM allows separate radius measurements to be derived from the RN and the total area (**Supplementary Fig. 1f**), and therefore the calculation of a derived halo radius. Radius measurements are calculated by fitting HIM output areas to circles (User Guide). However, we note that a significant minority of entities are elliptical. Application of an elliptical formula does not significantly change halo radius measurements (not shown), so we chose to perform circle formula based calculations throughout. Circles allow the whole area to be taken into consideration rather than just x- and y-axes, which like single visual radius measurements, are more affected by structural irregularities. In most cases we choose to present our results in terms of derived halo radius, as this reflects the theoretical chromatin loop size and has biological implications. If desired, and perhaps applicable to certain specific analyses, HIM allows different types of measurements to be made quickly and easily. For example RN radius or area measurements could be used to interrogate NM volume and compaction. Note that our standard combination of settings (HIM x55/15) systematically incorporates pixels at the outer halo edge that are not visible by eye (**Fig. 1e**), meaning halo measurements are systematically larger than those generated by eye.

Effect of flare The effect of flare from a bright RN on halo measurement was assessed using unexpanded 3T3 cell halos (treated only up to 0.5 M NaCl), in which histones are not extracted¹, and chromatin remains packaged within the nucleus. HIM x55/15 returned a halo radius that is approximately 5-fold less than that created by loop expansion, indicating a small but significant, systematic contribution to halo measurements (**Supplementary Fig. 1g**).

Using HIM to determine classifications Specialist HIMs were designed which use RN intensity to non-subjectively classify halos. Populations of cells processed by MFHR return two classes of product (**Fig. 1h**). Class I have defined RNs and class II have an ill-defined RN with poor structure and fail to return a value using HIM. Class I is further divided into class Ia (bright RN) and Ib (pale RN, **Fig. 1h**). Class Ia halos are defined as those in which >50% of the returned RN from local maxima is above 220 intensity. Class Ib halos have <50% of their RN above 220 intensity. Validation is shown in **Supplementary Fig. 2a**. RN HIM was trialled with different absolute intensity values (180-250 **Supplementary Fig. 2a**) and 220 chosen. For an example training set of visually defined Ia and Ib images, HIM RNx55/RN220 returned a value of 89% for class Ia, but only 7% for class Ib. Therefore using a cut off of 50% HIM RNx55/RN220 effectively separates class Ia and Ib halos and we show that HIMRNx55/RN220 classifies the whole 3T3 dataset the same as visual scoring (**Supplementary Fig. 2a right**). Nevertheless, other cell lines are less easy to classify by eye so RN HIM provides rapid, non-subjective classification by application of a constant intensity threshold.

HIM measurements for a panel of non-cancer cell lines Application of HIM x55/15 to a panel of cell lines returned significant, reproducible differences in both halo size and proportions of class Ia, Ib and II (**Supplementary Fig. 2b-d**), implying global differences in the frequency or nature of their MARs. We considered whether changes in halo size might reflect differing proportions of classes across populations, as we find that class Ia cells return slightly larger RN radius values and slightly smaller halo radius values than Ib cells using standard HIM x55/15 (**Supplementary Fig. 2b**). However the differences we observe in halo size across cell lines is not attributable to differing distribution within class I, because separate analysis returns similar trends (**Supplementary Fig. 2c**). In fact there is not a straightforward correlation between mean halo size and classification (compare **Supplementary Fig. 2c** and **2d**). For example, NHU and MCF10A have a similar percentage of class Ia cells (78% and 88% respectively), but different mean halo radius (16 μm and 13 μm respectively), while BJ-hTERT has only 42% class Ia cells, and a mean halo size similar to MCF10A. The differences in halo parameters that we observe across a panel of non-cancer cell lines therefore shows that choice of 'normal' comparison is highly important.

Customization of HIM for MSCs Cell types respond to MFHR differently, in some cases requiring HIM thresholds to be fine-tuned for particular analyses. Mesenchymal Stem Cells (MSCs)² were observed to produce MFHR images with pale RNs, requiring the RN threshold criteria to be adapted so that it supports analysis across the whole diverse series. Different

RN values, based on range from local maxima (where $x=55, 70, 75, \text{ or } 100$) were compared for measurement of MSC1 and MSC3 cell lines (**Supplementary Fig. 3b**). The HIM default threshold ($x55$) gave a smaller than visual measurement for both cell lines, while RN $x75$ gave a similar value to visual assessment (100.7% for MSC3). MSC1 RN measurements are still somewhat smaller than visual measurements at $x75$, which will lead to slight overestimation of halo size. In fact several sets of HIM settings were trialled on the MSC series data (**Supplementary Fig. 3c**). HIM $x75/x180$ (**Fig. 2b**) was used to derive a halo measure in which both parameters are related to RN intensity. For this analysis, the range settings for outer threshold ($x180$) was chosen to support inclusion of a greater proportion of cells across the series. Outer range settings higher than 180 incorporate smaller percentages of the population, but still report differences in halo measurements between MCS1 and 3 (**Supplementary Fig. 3c, d**). A different version of HIM ($x75/15$, **Fig. 2c**) uses an outer threshold with absolute pixel intensity of 15, which reflects the point at which intensity increases over background, where background is set at 5% AUC for a training population (**Fig. 1e**). Here outer threshold is unaffected by RN intensity and reports only on differences in RN and halo size. We remind readers that data collected using different thresholds should not be compared. For example, mean halo measurements in figure 2c cannot be directly compared to figure 2b, except to evaluate the effect of the different settings.

Customisation of classification HIM for MSCs To establish suitable parameters for classification of MSCs by HIM, data collected using different absolute RN pixel intensity thresholds were compared to classifications by eye for a representative set of images for MSC1 (**Supplementary Fig. 3e, f**). Those that were visually scored as class Ia, but by HIM were scored as class Ib, are defined as false Ib, and those visually scored as Ib, but by HIM scored as Ia, are defined as false Ia. For MSC1, classification based on a 50% cut off, using intensity above 180 or 200 caused significant percentages of false Ia images. Likewise, above 230 produced a significant percentage of false Ib images (**Supplementary Fig. 3f**). We chose 220 intensity as our parameter, as this minimized 'false' classification with the training set, and confirmed that this is suitable across the full range of the MSC series (**Supplementary Fig. 3g**), before application to test populations.

Validation of biological differences As with all analysis methods that image slides prepared in different sessions, we considered whether biological differences could be seen above the level of variability between replicate experiments. To illustrate this, frequency distributions were plotted for halo size measurements generated using HIM $x75/x180$ from MSC cell lines, for complete data sets (**Supplementary Fig. 4a**) and individual biological

and technical replicates (**Supplementary Fig. 4b, c, d**), and variance calculated using ANOVA (**Supplementary Fig. 4e**). Graphs show that individual replicates from the same cell line overlay well and are more similar to each other than to data sets from a different cell line, compare MSC1 and 2 (**Supplementary Fig. 4b**) and MSC4 and 5 (**Supplementary Fig. 4c**). Furthermore, individual data sets return the same results as the mean of each set of replicates (**Supplementary Fig. 4a, Fig. 2b**). ANOVA results confirm that MSC1 halo size data set is statistically different from MSC2, and that MSC4 is statistically different from MSC5, but MSC2 is not different to MSC4. Overall, this shows that variation inherent in preparation conditions is far less than biological differences between cell lines.

In addition, we processed and imaged MSC1/MS4 and MSC4/MS5 as pairs, in order to ensure identical reagents and process. As expected, we find the same statistical differences as when processed independently (compare **Supplementary Fig. 4f** and **Fig. 2b**). Taken together this allows us to conclude that the differences we observe between cell lines is not due to slide to slide variability but statistically robust biological differences due to cell type.

Supplementary Table 1: Versions of HIM, with their applications

HIM title	Usage
HIM x55/15	Halo size for non-cancer and cancer cell lines Defines RN (local maxima less 55) and outer threshold (intensity 15) areas
HIM x75/15	Halo size for MSC series Defines RN (local maxima less 75) and outer threshold (intensity 15) areas
HIM x75/x180	Halo size for MSC series (includes effect of RN intensity) Stability for MSC series Defines RN (local maxima less 75) and outer threshold (local maxima less 180) areas
HIM x55/x240	Stability for non-cancer and cancer cell lines Defines RN (local maxima less 55) and outer threshold (local maxima less 240) areas
HIM RNx55/RN220	Classification for non-cancer and cancer cell lines Defines the RN percentage above 220 intensity
HIM RNx75/RN220	Classification for MSC series Defines the RN percentage above 220 intensity

User Guide: Halo Image Macro for ImageJ

File output HIM opens each image file, selects a region of interest (ROI) within each image based on the 'RN threshold', measures the RN area and saves a copy of the new file, with the ROI shown, in the 'RN threshold' folder. This is repeated for the 'outer threshold', saving the new file in the appropriate folder. The 'setBatchMode' command in the HIM code stops the visual opening and processing of each file. This command may be removed to visualize the steps and allow troubleshooting.

The output for each file is a RN threshold analysis picture, an outer threshold analysis picture, and area measurements for each. Measurements are initially recorded in the 'Results' dialogue box. HIM then matches RN and outer area measurements for each cell and exports the data to a .csv (comma-separated values) file which can be read by excel. Users should then save this file as a .xlsx file or other excel file type as some excel features are not compatible with .csv files.

Matching RN and outer measurements RN and outer area measurements from the same cell are matched by using x- and y- positional information for the centre of each ROI. The HIM queries a possible pair (from within the same image) and if the x- and y- centre coordinates of the RN and outer differ by less than 5% of the square root of the total image area, measurements are linked with the outer data moved to the same row as the RN data. If the pair fail to fulfil this criteria, HIM will query any other RN measurements from the image (ie if multiple cells are present on the image) to see if they match with the outer measurement. If no matching RN is found, the outer measurement data are not moved and they remain on their own row of the output .csv file. HIM is therefore capable of dealing with images with multiple cells which may or may not record both an RN and outer measurement and which may not be recorded in the same order. However, users are advised to prepare slides using a cell plating concentration that does not result in excessive cells per image as it is more likely that cells will be touching. HIM cannot discriminate a pair of touching cells from one single cell and images should be quickly checked for any such occurrences.

In addition, when HIM has finished processing each file within the source folder, any images where a RN and outer pair was not found for all ROIs will be listed in a dialogue box titled, "Files requiring manual curation". Images will also be listed here for which no RN, or no outer was detected.

Images which 'fail' HIM also checks any outer measurements which 'fail' (see description of stability measurements and class II cells) in that the outer measurement occupies more than 80% of the image area. This happens typically for pale cells when outer measurements are measured using the local maxima less x method eg when unstable cells decay during stability analysis. Outer measurements that are larger than 80% of the image area are replaced by 'fail' under outer area measurement heading. This is applied to all RNs on an image for which an outer area measurement is classified as a fail.

Results column headings For cells with a matched RN and outer measurement, the cell returns recordings under the following headings;

Label - this is the image name followed by RN indicating a unique RN

Area - RN area

X - central x- position of RN ROI - used for positional information

Y - central y- position of RN ROI - used for positional information

Image No. - this refers to the numbered RN on the RN threshold analysis image saved in the 'RN' folder and maybe used to match cell data back to the original image

Outer Area - matching outer area measurement

Outer X - central x-position of outer ROI - used for positional information

Outer Y - central y-position of outer ROI - used for positional information

Outer Image No. - this refers to the numbered outer on the outer threshold analysis image saved in the 'Outer' folder. Note: outers from different images may have the same number, this is due to results being recorded and then being moved to the appropriate RN row. Therefore, if wishing to refer back to outer threshold images users should check the image name and outer number carefully.

Headings are slightly different for classification HIM output with outer replaced by absolute RN. This refers to the ROI generated using an absolute pixel intensity threshold rather than one related to the local image maxima.

To run HIM:

- Install ImageJ from <http://rsb.info.nih.gov/ij/download.html>. HIM is compatible with ImageJ for Mac OS X or Windows, version 1.47o or later. Previous versions do not accept strings in the Results table data columns (for example, used here for 'fail').

- Download appropriate HIM .txt file from supplementary files, into a dedicated folder. If desired, replace default threshold settings (x55/15), chosen after calibration to your cell type.
- Create a source folder for MFHR images that are to be analysed, and three destination folders for 'RN threshold' and 'outer threshold' respective output pictures and a folder for excel readable files.
- Populate source folder with a set of MFHR image files. We use 'TIFF For Publication' files, derived from Openlab image acquisition software for Mac, however HIM will analyse any high resolution ImageJ compatible file types. Please note, the first image to be analysed must contain at least one cell otherwise HIM will not return any information for that image. Images without a cell are tolerated after the first image and the HIM will return *no RN and *no outer for such images.
- Open ImageJ and load HIM with the command:
 Plugins –
 Macros –
 Install...
 Then select the appropriate HIM .txt file.

Run HIM in ImageJ with the command:

Plugins –
 Macros -
 then select the HIM you have just loaded.

When measuring different sets of images with the same HIM, the HIM file only needs loading at the beginning of the session. However, if changing between different HIMs then they will need to be reloaded each time.

- After selecting the HIM to run, a dialogue box opens. Select the appropriate source folder, then when prompted, select the RN and outer threshold destination folders. Finally, select the results folder and type your desired name for the .csv results file. HIM then runs without further prompting.
- When HIM is running, the ImageJ results table is visible. However, once the HIM saves these data into the .csv file the results table closes. On completion of HIM, a

dialogue box entitled "Files requiring manual curation" appears highlighting any files that proved difficult to analyse, either due to *no RN or * no Outer being measured, or if pairs of RN and outers could not be linked. Upon completion the user should check these images and respective RN and outer threshold analysis files and adjust the .csv file accordingly. Output images should also be checked for joined cells, cells cut by the edge of the picture and occasional extraneous particles which should all be removed. This can also be done at the image acquisition stage, though random acquisition is preferred.

- Calculate halo radius using the formula;

$$\text{Halo radius} = \left\{ \left(\frac{\sqrt{\text{outer area}'}}{\pi} \right) - \left(\frac{\sqrt{\text{RN area}'}}{\pi} \right) \right\} \times c$$

where c is a conversion factor between pixels and μm

Determine conversion factor for your imaging equipment and software using automated scale bar functions, or directly by imaging a graticule under the same conditions used to image halos. Calibration between pixels and micrometers should be made following consistent file transfer protocols, as pixel measurements are not always consistent between software.

Micrometer measurements can be converted to an estimate of chromatin loop size in kilobases using conversion factors published previously. These range from $1 \mu\text{m} = 3 \text{ kbp}^{3,4}$, to $1 \mu\text{m} = 2.3 \text{ kbp}^5$. We chose to use the former, based on 10.4 bp per helical turn in B-form DNA⁶ with a helical turn of 3.4 nm^7 . Note that radius values should be doubled to reflect the fact that loops are composed of two radii.

These steps take about 5 minutes per coverslip including ~1 minute of macro running time.

Analysis specific to classification The classification HIM generates the standard RN area measurement based on local maxima and a second RN area based on an absolute intensity threshold, from which a % is derived. If this is above 50%, the RN is designated as class Ia, if this is equal to or below 50%, the RN is designated as class Ib.

Analysis specific to stability measurements Data from stability measurements can be presented as time to fail, or percentage of surviving halos as described earlier.

Manual execution Instructions for manual execution of the steps carried out automatically by HIM x55/15 are detailed below (direct instructions in italics). Where both thresholds are relative to the local maxima (for example HIM x55/x240), outer threshold is measured in the same way as RN using appropriate threshold. This does not include the matching of RN and outer measurements which can be found in the HIM .txt file.

Open file in ImageJ

Select ImageJ: Image: Type: 8-bit

This converts the image to greyscale 8-bit values from RGB.

ImageJ: Process: Find maxima

Dialogue box opens, *select Noise tolerance 55, Maxima within tolerance, nothing ticked.*

This results in a new picture, and selects the pixels within a tolerance of 55 from the local maximal intensity of the image. The area in white will be measured.

ImageJ: Process: Binary: Close

The individual pixels selected will then be closed as an ROI.

ImageJ: Image: Adjust: Threshold

In Threshold dialogue box, *Set thresholds at 255, default, red, box not ticked, Apply, close box*

ImageJ: Analyze: Analyse Particles

In dialogue box, *Size 3000-Infinity, Pixel units ticked, Circularity 0.00-1.00, Show Outlines, Only Display results and Exclude on Edges ticked.*

This results in area measurements taken for white areas bigger than 3000 pixels.

Save new picture in Threshold RN, Close all open files except raw image.

To measure outer threshold area...

Image: Adjust: Threshold...

In Threshold dialogue box, *Set*, in Set Threshold Levels dialogue box *Lower Threshold Level at 15, Upper Threshold Level at 255, ok.* In Threshold dialogue box, *default, red, Dark background ticked, apply, close box.* In NaN Background dialogue box *ensure Background Pixels to NaN is not ticked, ok.*

Note that this results in an absolute pixel intensity threshold unlike that for RN.

ImageJ: Process: Binary: Convert to Mask

ImageJ: Process: Binary: Close-

ImageJ: Analyze: Analyze Particles

In dialogue box, Size 3000-Infinity, Pixel units ticked, Circularity 0.00-1.00, Show Outlines, Only Display results and Exclude on Edges ticked.

Save new picture in Threshold Outer, Close all open files.

Technical tips for MFHR processing and image generation

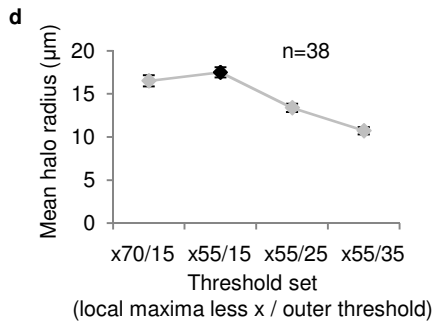
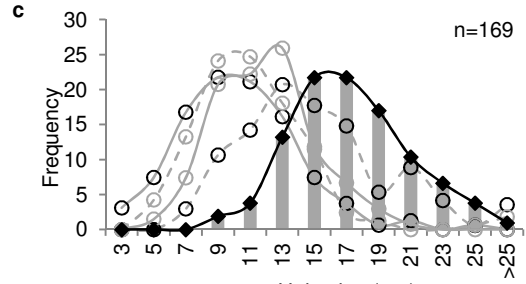
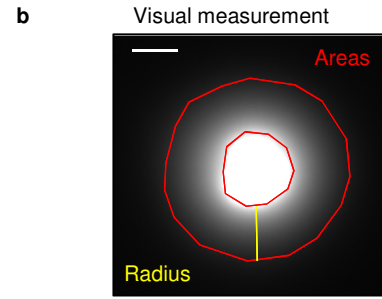
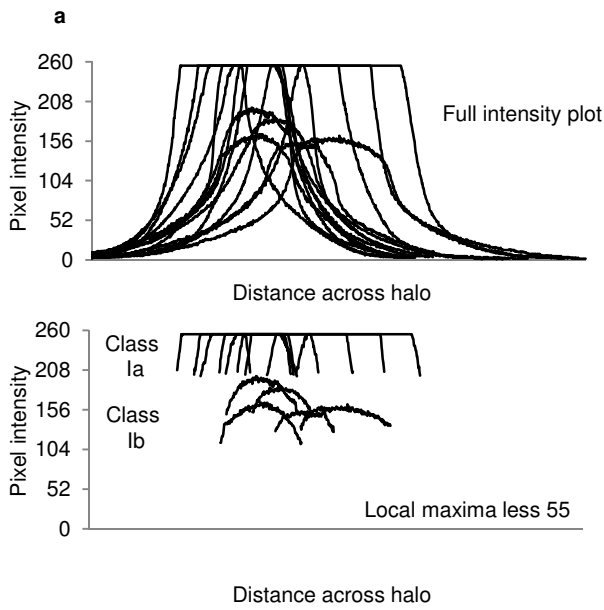
These are provided to help minimize other sources of variability.

- The pH of buffers should be checked carefully as this can affect halo stability
- Buffers should be made up in advance and stored in aliquots at -20°C, to generate complete data sets with one batch. Working aliquots may be kept at 4°C for one week
- Buffers should be pre-cooled on ice, and all processing performed on ice
- Process and image one coverslip at a time
- Carefully lower coverslips into solutions to prevent loss of cells. Do not pipette buffers onto coverslips.
- Standardise distance from cells to UV light source
- Seal mounted coverslips with clear nail varnish to prevent buffer flow
- Keep slides in the dark during the development period
- Collect images within a limited time period (we use 10 minutes) to prevent analysis of degraded halos.
- Minimize time between visualization of a halo and image capture
- Take care not to re-image areas of the coverslip that have already been exposed to microscope light.
- For class analysis no halo should be excluded from image capture. These image sets can also be used for size analysis. If only size analysis will be performed, joining halos can be excluded at image capture, since HIM cannot measure these halos.
- Exposure time, and RN and outer thresholds should be set using a training set.

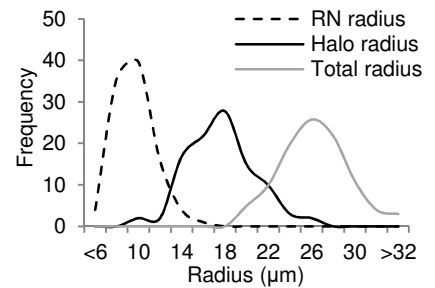
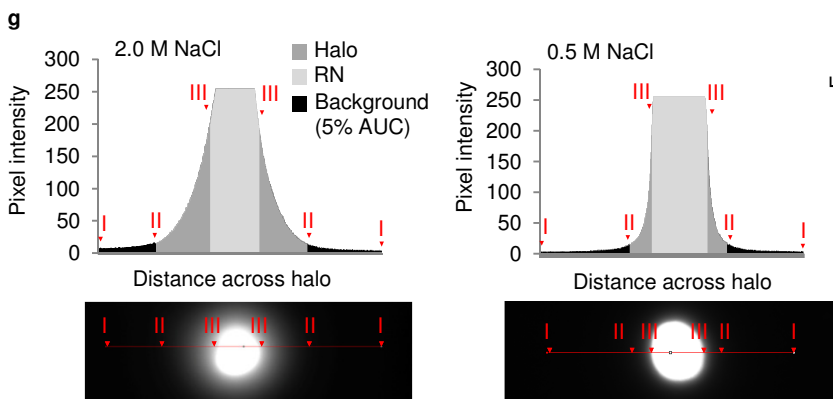
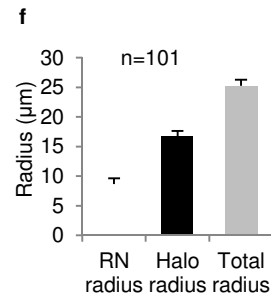
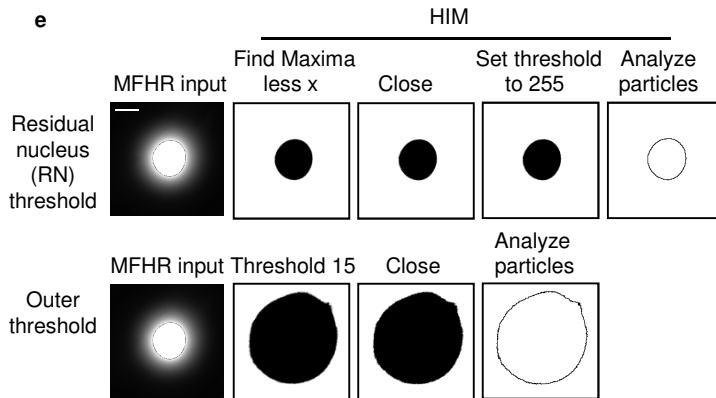
References for supplementary material

- 1 Hesketh, E. L., Knight, J. R. P., Wilson, R. H. C., Chong, J. P. J. & Coverley, D. Transient association of MCM complex proteins with the nuclear matrix during initiation of mammalian DNA replication. *Cell Cycle* **14**, 333-341, doi:10.4161/15384101.2014.980647 (2015).
- 2 Funes, J. M. *et al.* Transformation of human mesenchymal stem cells increases their dependency on oxidative phosphorylation for energy production. *Proc Natl Acad Sci U S A* **104**, 6223-6228, doi:10.1073/pnas.0700690104 (2007).
- 3 Buongiorno-Nardelli, M., Micheli, G., Carri, M. T. & Marilley, M. A relationship between replicon size and supercoiled loop domains in the eukaryotic genome. *Nature* **298**, 100-102 (1982).
- 4 Vogelstein, B., Pardoll, D. M. & Coffey, D. S. Supercoiled loops and eucaryotic DNA replicaton. *Cell* **22**, 79-85 (1980).

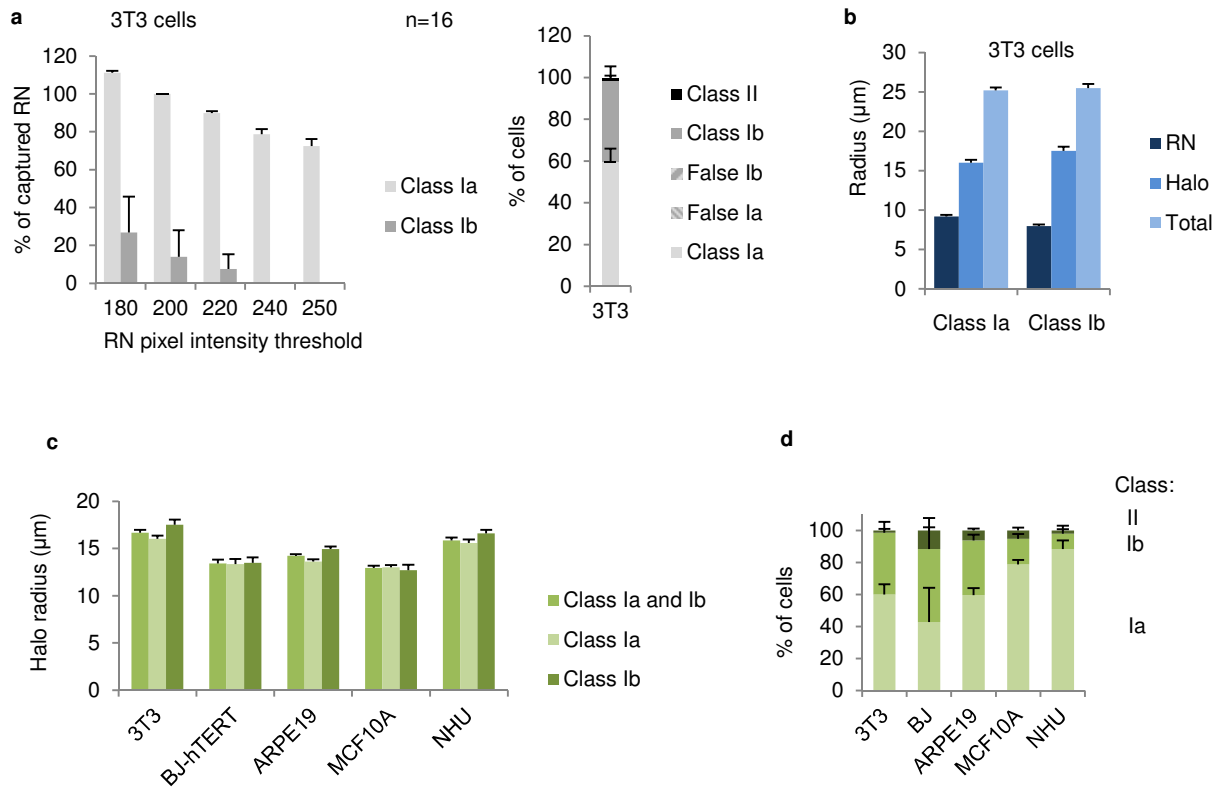
- 5 Lemaitre, J. M., Danis, E., Pasero, P., Vassetzky, Y. & Mechali, M. Mitotic remodeling of the replicon and chromosome structure. *Cell* **123**, 787-801, doi:10.1016/j.cell.2005.08.045 (2005).
- 6 Wang, J. C. Helical repeat of DNA in solution. *Proc Natl Acad Sci U S A* **76**, 200-203 (1979).
- 7 Watson, J. D. & Crick, F. H. Molecular structure of nucleic acids; a structure for deoxyribose nucleic acid. *Nature* **171**, 737-738 (1953).



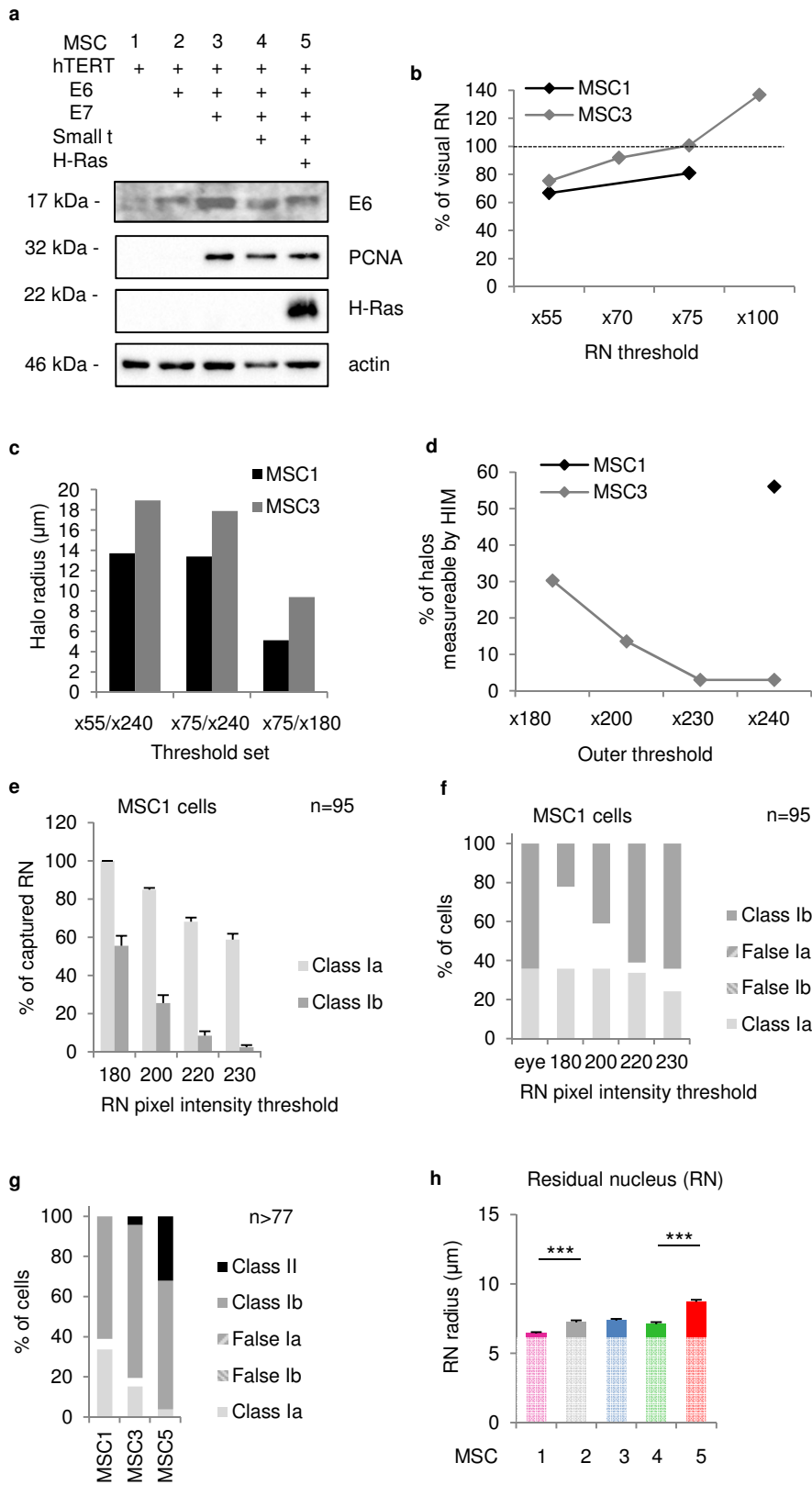
Analysis	Halo size (μm)		
	User	Computer	Method
visual	1	1	vertical line
	1	2	vertical line
	2	2	vertical line
HIM	1	1	area
	1	1	HIM
	1	2	HIM



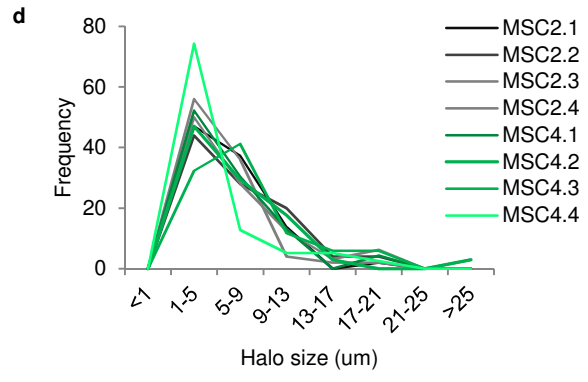
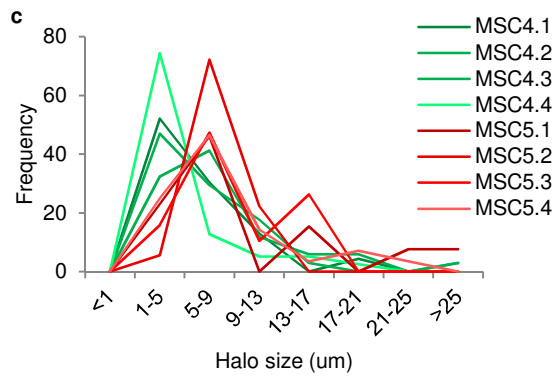
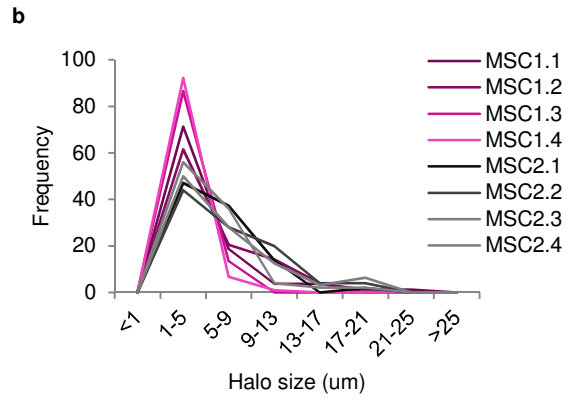
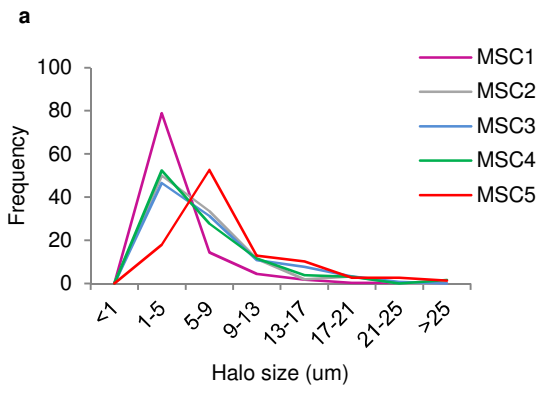
Supplementary Figure 1



Supplementary Figure 2

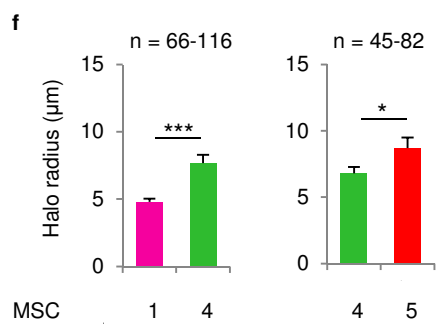


Supplementary Figure 3



e

	One-Way ANOVA
MSCh1 - 5	$F_{(4, 853)} = 30.35, p < 0.001$
MSCh1, 3, 5	$F_{(2, 567)} = 62.34, p < 0.001$
MSCh2 - 4	$F_{(2, 442)} = 1.15, p = 0.32$
MSCh1 - 2	$F_{(1, 491)} = 43.15, p < 0.001$
MSCh2 - 3	$F_{(1, 313)} = 2.31, p = 0.13$
MSCh3 - 4	$F_{(1, 285)} = 1.05, p = 0.31$
MSCh4 - 5	$F_{(1, 206)} = 12.06, p < 0.001$



Supplementary Figure 4